Long-Term Spin State Storage Using Ancilla Charge Memories

Harishankar Jayakumar,[1] Artur Lozovoi[●],[1] Damon Daw[●],[1] and Carlos A. Meriles[●][1,2,*]

[1]*Department of Physics, CUNY-City College of New York, New York, New York 10031, USA*
[2]*CUNY-Graduate Center, New York, New York 10016, USA*

We articulate confocal microscopy and electron spin resonance to implement spin-to-charge conversion in a small ensemble of nitrogen-vacancy (NV) centers in bulk diamond and demonstrate charge conversion of neighboring defects conditional on the NV spin state. We build on this observation to show time-resolved NV spin manipulation and ancilla-charge-aided NV spin state detection via integrated measurements. Our results hint at intriguing opportunities in the development of novel measurement strategies in fundamental science and quantum spintronics as well as in the search for enhanced forms of color-center-based metrology down to the limit of individual point defects.

Paramagnetic color centers in semiconductors are presently capturing widespread interest as versatile qubits for nanoscale sensing and quantum information processing [1,2]. In particular, optical access to individual color centers coupled to single-electron spin control and millisecond-long coherence spin lifetimes have led to stunning demonstrations of entanglement and quantum logic in diamond and other wide-band-gap materials [3,4]. Although the prevalent approach in much of this work focuses on the relationship between the defect spin state and the photons it emits or absorbs, recent efforts have been expanded to explore the virtual atom's "valence" charge carriers as a means for transporting quantum information [5], creating local environments protected against spin decoherence [6], or enabling more convenient forms of defect spin readout [7]. For example, the use of spin-to-charge conversion schemes has led to demonstrations of electrical spin qubit detection in diamond [8–10] or as a route for spin-polarized carrier injection [5].

Here we combine magnetic resonance and multicolor confocal microscopy to alter the charge state of a small ensemble of negatively charged nitrogen-vacancy (NV$^-$) centers in diamond conditional on their spin state. Successive cycles of ionization and recombination of the "qubit" NVs respectively produce free electrons and holes, which we subsequently capture via an ensemble of neighboring carrier-type-selective traps. Adapting this ancilla-aided integrated detection (AID) strategy to time-resolved measurements, we demonstrate basic building blocks of NV$^-$ spin control for different trap types. Although under the present conditions standard photoluminescence readout still proves more sensitive, we expose through experiment and modeling a broad parameter space that could be potentially exploited not only to boost sensitivity beyond existing techniques, but also, more generally, as a platform for applications where the charge carrier itself serves as a flying qubit.

The cartoon in Fig. 1(a) summarizes our starting working geometry, comprising small ensembles of NV centers surrounded by a larger set of charge traps [11]. The latter take the form of point defects whose fluorescence changes (e.g., from dark to bright or vice versa) upon capture of a carrier. For the present studies, we first use silicon-vacancy (SiV) centers, whose charge state can be controlled with light pulses of suitable wavelength [12,13]. Though surface effects [14–17] and/or carrier tunneling [18] can render the charge state of defects unstable, SiV centers at moderate concentrations (∼0.1 ppm in the present sample) are known to feature long-lived charge states and, hence, serve as classical memories with virtually unlimited storage time in the dark [19].

The mechanism underlying spin-conditional ionization of the NV—a spin $S = 1$ defect featuring triplet ground and excited states [20]—can be understood with the help of the energy diagram in Fig. 1(b). Optical excitation induces a spin-preserving transition within the triplet manifold, followed by radiative decay. Intersystem crossing to a manifold of intermediate singlet states (where $S = 0$) is more likely when the initial NV triplet state is $|m_S = \pm 1\rangle$, thus leading to spin-selective shelving (the basis for NV spin optical readout [21]). At sufficiently high laser powers, photon absorption during the excited triplet lifetime (∼10 ns) propels the NV$^-$ excess electron into the conduction band, hence changing the charge state of the NV into neutral [22]. When the illumination interval is comparable with the shelving time (∼100 ns), the above two-step photon process is more probable for the $|m_S = 0\rangle$ state—relatively immune to intersystem crossing—thus leading to spin-selective electron injection into the conduction band. This spin-to-charge conversion (SCC)
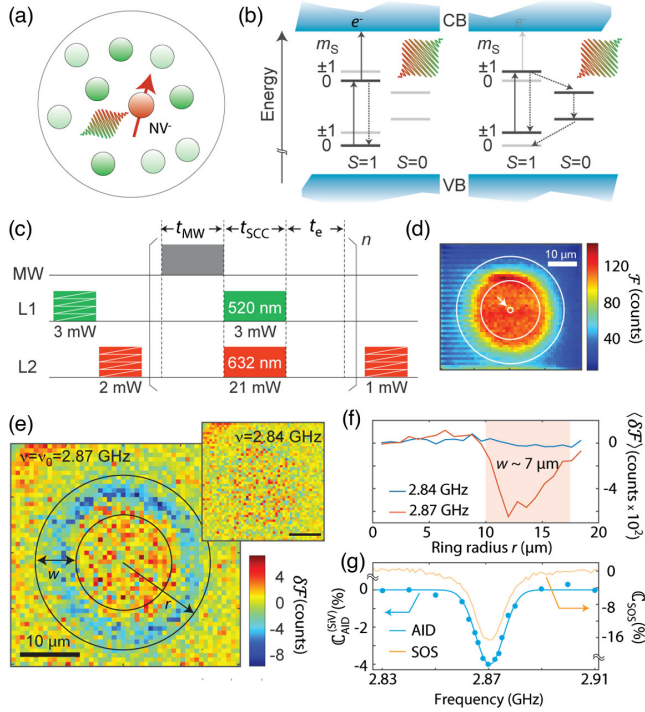
FIG. 1. Charge storage of NV$^-$ spin state. (a) Ancilla charge traps change their fluorescence upon capture of carriers produced by NV ionization and recombination. (b) Schematics of NV charge photoionization dynamics. (c) Experimental protocol. Zigzags denote charge initialization and readout raster scans, each one demanding 40 and 5 s, respectively. (d) SiV$^-$-selective fluorescence image $\mathcal{F}$ upon use of the protocol in (c) for an integration time $t_{\text{int}} = n(t_{\text{MW}} + t_{\text{SCC}} + t_e) = 10$ s with $t_{\text{MW}} = t_{\text{SCC}} = 100$ ns and $t_e = 1$ μs. The white arrow points toward the illuminated area; the medium and outer circles demark the region of maximal spin contrast. (e) Differential SiV$^-$ fluorescence patterns $\delta\mathcal{F} \equiv \mathcal{F}_{\text{on}} - \mathcal{F}_{\text{off}}$; subscripts indicate MW is resonant with (2.87 MHz, main) or far detuned from (2.84 MHz, inset) the NV$^-$ ground-state crystal-field frequency v_0. (f) SiV$^-$ differential fluorescence averaged over a 1-μm-wide ring of variable radius r for the on- and off-resonance images in (e). (g) NV$^-$ magnetic resonance spectra using SiV-AID or SOS.

process [7,23–25] underlies recent demonstrations of electrical spin readout [8,9], down to individual NVs [10].

In our experiments, we first study a [100]-type 1b diamond crystal simultaneously hosting NVs, SiVs, and nitrogen impurities with approximate concentrations of 10^{-2}, 10^{-1}, and 1 ppm, respectively. Figures 1(c)–1(e) lay out the fundamentals of our spin storage protocol: We use multiple red (632 nm) laser scans to charge initialize NVs and SiVs within a 40×40 μm^2 area into a non-fluorescent state [26]. We then cycle the NVs at the center point of this region between their neutral and negative charge states via simultaneous green (520 nm) and red laser pulses (of duration $t_{\text{SCC}} = 100$ ns). The latter are separated by (optional) microwave (MW) pulses, whose length ($t_{\text{MW}} = 100$ ns) and frequency (2.87 GHz) are adjusted so as to invert the populations of the $|m_S = 0\rangle$ and

$|m_S = \pm 1\rangle$ states of the ground triplet [Fig. 1(c)]. Each event of NV ionization (i.e., NV$^- \rightarrow$ NV^0) and recombination (i.e., NV$^0 \rightarrow$ NV$^-$), respectively, results in the generation of a free electron and a hole, which subsequently diffuse away from the illumination point to be ultimately captured by a neighboring trap. Under these conditions, SiVs exhibit a one-way transformation into the negatively charged, bright state [26], thus leading to the formation of a fluorescent disk centered around the point of optical excitation [Fig. 1(d)]. Note that identical numbers of electrons and holes are injected during multiple repetitions of the qubit control protocol, hence allowing one to store the qubit spin state via the capture of one carrier type or the other, provided the traps are predominantly sensitive to one type only, the case for SiV [26].

For $n \gg 1$ cycles of ionization-recombination, the integrated number of carriers—and, correspondingly, the average radius of the SiV$^-$ disk in the ensuing confocal image—is larger when the MW field is off (because the NV$^-$ spin state is $|m_S = 0\rangle$, where ionization is more likely). We expose this spin-dependent contrast in Fig. 1(e), where we subtract the SiV fluorescence patterns obtained with and without resonant MW acting on the NV crystal-field transition after an "integration" time $t_{\text{int}} = n(t_{\text{MW}} + t_{\text{SCC}} + t_e)$, where t_e is the wait time between successive cycles. This trap-encoded spin signal (SiV-AID) takes the form of a concentric dark ring, absent when the MW is detuned off resonance [left and right panels in Fig. 1(e), respectively].

To quantify the effect at arbitrary MW frequencies ν, we first calculate the integrated SiV$^-$ fluorescence $\langle\mathcal{F}\rangle(r_i, \nu) = \sum_j \mathcal{F}(\varphi_j, r_i, \nu)$ over all angles φ_j along concentric, 1-μm-wide rings of increasing radii r_i. We subsequently use this radial distribution to determine the contrast $\mathbb{C}_{\text{AID}}^{(\text{SiV})}(\nu) = 2[I_{\text{on}}(\nu) - I_{\text{off}}]/[I_{\text{on}}(\nu_0) + I_{\text{off}}]$, where $I(\nu) = \sum_i \langle\mathcal{F}\rangle(r_i, \nu)$ is the integrated fluorescence, here restricted to a ring of width $w \approx 7$ μm around $r \approx 14$ μm for optimal SNR [see Fig. 1(f)]. In the above expression, ν_0 is the NV$^-$ spin resonance frequency, and the label indicates on or off MW. Using these definitions, Fig. 1(g) shows the SiV-AID magnetic resonance spectrum of NV$^-$. We find it to be in good agreement with that obtained from collecting the NV$^-$ spin-dependent photoluminescence, the most common readout protocol here referred to as standard optical sensing (SOS).

Given the unlimited lifetime of trapped charge states at these defect concentrations [19,27], signal integration can be carried out over a broad time interval, here ranging from 50 ms to 10 s. Figures 2(a) and 2(b), respectively, show some snapshots of the evolving SiV charge distribution within this temporal span, alongside the integrated spin signal at each of these times. Furthermore, the present approach can be easily adapted to time-resolved measurements of the spin qubit. A first demonstration is presented in Fig. 2(c), where we use the sequence in Fig. 1(c) with a
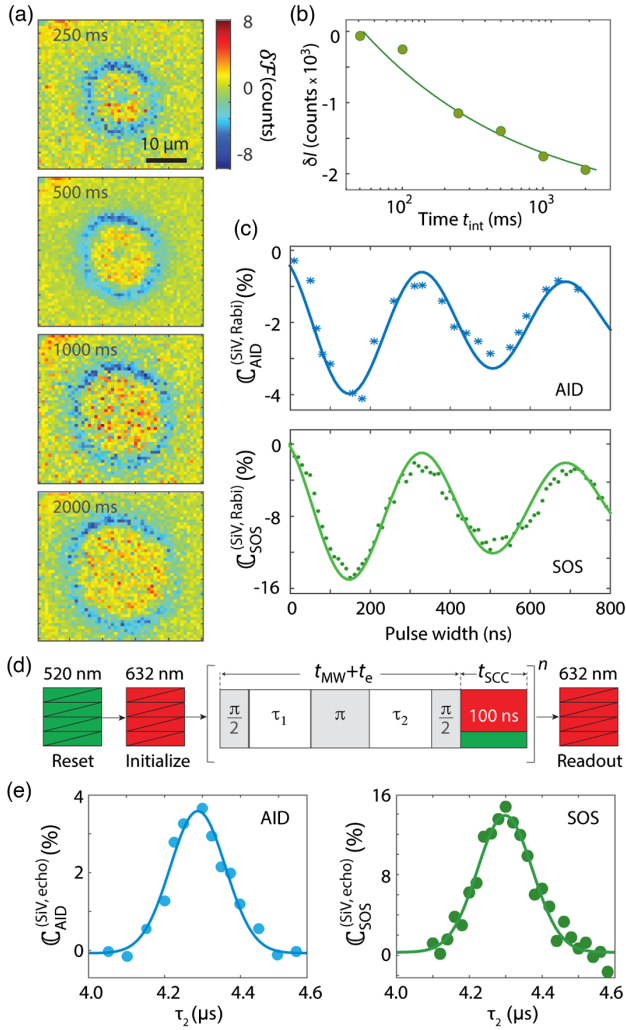
FIG. 2. Time-resolved, charge-encoded NV$^-$ spin dynamics. (a) SiV$^-$ differential charge patterns for different integration times. (b) On-resonance SiV-AID signal $\delta I(\nu_0)$ as a function of the integration time t_{int}. (c) NV$^-$ spin Rabi signal using the protocol in Fig. 1(c) for resonant MW pulses of variable duration or using SOS readout (upper and lower plots, respectively). (d) AID-adapted NV$^-$ spin-echo sequence; SCC denotes spin-to-charge conversion using simultaneous 100-ns-long red and green optical pulses, as in Fig. 1(c). (e) Measured AID (left) and SOS (right) NV spin Hahn-echo signals. In all plots, solid traces are guides to the eye.

variable MW pulse duration to measure the NV$^-$ spin Rabi response. A more involved scheme is shown in Fig. 2(d), this time adapted to measure the NV$^-$ spin echo signal [Fig. 2(e)].

While SiVs serve as convenient traps for the present application, they are certainly not the only type of defects one can resort to. One immediate possibility are NV centers, effectively trapping holes when negatively charged but displaying a poor electron capture cross section in the neutral state [26]. Extending the results above, we implement NV-encoded spin storage using ancilla NVs

sufficiently removed from the point of laser illumination. Figure 3(a) shows the experimental protocol: Unlike in Fig. 1(c), this time we use a green laser scan to charge initialize the area around the point of optical excitation into a majority of negatively charged NVs. For these experiments, we use a SiV-free diamond crystal with nitrogen and NV concentrations of 1 and 10^{-2} ppm, respectively. Though convenient to enhance sensitivity, this modified diamond composition is not mandatory, as the SiV$^-$ fluorescence can be selectively filtered out from the recorded emission spectrum [26]. Figure 3(b) displays the fluorescence $\mathcal{G}$ from ancilla NVs emerging after multiple repetitions n of the SCC protocol and a red readout scan: Surrounding the central bright spot, we observe the formation of a pronounced dark halo, indicative of ancilla transformation to a majority-neutral charge state via the capture of holes diffusing from the point of illumination [inner white circle in Fig. 3(b)].

To reveal the spin state of the qubit NVs (i.e., the NVs directly exposed to the green or red beams), we subtract the fluorescence patterns $\mathcal{G}_{\mathrm{on/off}}$—this time produced by the ancilla NVs—with and without MW. We find a nonzero difference only when the microwave is resonant with the

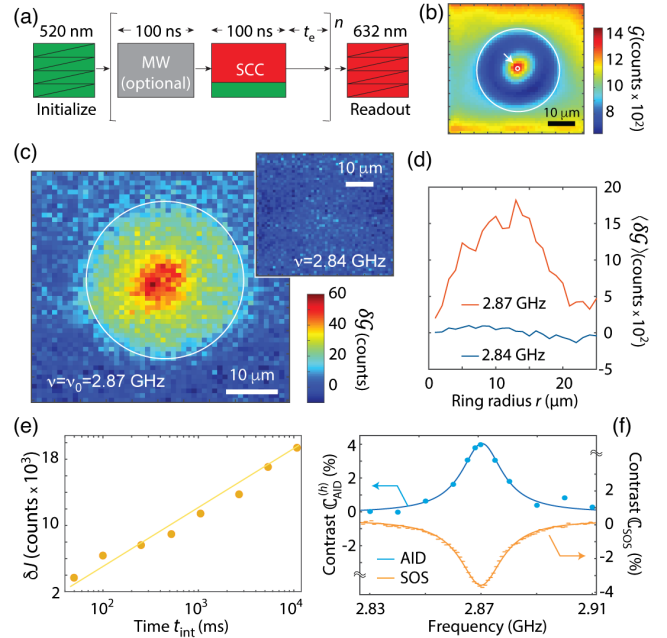FIG. 3. NV-aided long-term spin state storage. (a) Experimental protocol; $t_e = 1 \ \mu$s is the wait time between successive cycles. (b) NV$^-$ fluorescence image using the scheme in (a). Excluding the initialization and readout scans, the total signal integration time amounts to 10 s. (c) NV$^-$ differential fluorescence images $\delta\mathcal{G} \equiv \mathcal{G}_{\mathrm{on}} - \mathcal{G}_{\mathrm{off}}$ using resonant (main) and off-resonant (inset) MW. (d) NV$^-$ differential fluorescence averaged over 1-μm-wide rings of variable radii r for resonant or detuned MW (red and blue traces, respectively). (e) On-resonance NV-AID signal $\delta J(\nu_0)$ as a function of the integration time t_{int}. (f) NV$^-$ spin resonance spectra as determined using NV-AID or SOS (blue and yellow dots, respectively). In all plots, solid traces are a guide to the eye.

NV$^-$ crystal field transition [left image in Fig. 3(c)], thus yielding an NV-encoded integrated spin signal (NV-AID). Contrary to Fig. 1(e), the fluorescence change $\delta\mathcal{G} \equiv \mathcal{G}_{on} - \mathcal{G}_{off}$ is positive, corresponding to fewer ancilla NVs transitioning to neutral when the MW is on; the latter, in turn, agrees with the notion of less frequent NV$^-$-ionization-recombination cycles due to MW-induced NV$^-$-state shelving in the singlet manifold. Interestingly, the maximum fluorescence difference is found near the point of illumination, indicative of a spin-dependent NV$^-$ concentration under optical excitation. Note, however, that this contribution has a negligible impact on the radial fluorescence distribution $\langle\delta\mathcal{G}\rangle$—vanishing near the origin, Fig. 3(d)—and, thus, on the integrated NV-AID signal $\delta J(\nu) = \sum_i \langle\delta\mathcal{G}\rangle(r_i, \nu)$. As a matter of fact, we measure a time growth [Fig. 3(e)] comparable to that observed above for silicon vacancies [Fig. 2(b)]. Likewise, we attain good agreement between the NV-AID and SOS spectra [Fig. 3(f)].

To better understand the range of conditions where the use of AID can be advantageous, we model spin-to-charge conversion via the stochastic variables q_j, $j = 0, 1$, respectively, associated with the probabilities of generating a charge carrier when the initial NV$^-$ state has spin projection $|m_S| = j$. Using $\langle\rangle$ and δ^2 to, respectively, denote mean values and variances, we find that the detection sensitivity after n repeats is given by [11]

$$\eta_{AID} = \frac{\sqrt{t_{AID}}\sqrt{\sum_j[\delta^2(k_a v_j) + (1-\lambda)\langle k_a\rangle^2\langle v_j\rangle^2]}}{\sqrt{\lambda}\langle p\rangle\left|\langle q_0\rangle - \langle q_1\rangle\right|\langle k_a\rangle}, \quad (1)$$

where $\langle\lambda\rangle$ is the fraction of carriers captured by the ensemble of useful ancilla traps (i.e., those that can be subsequently read out), $\langle k_a\rangle$ is the average number of photons collected during charge readout of an ancilla, and $v_j \equiv pq_j + w$ is a stochastic variable describing ancilla trap activation. In the latter expression, w denotes contributions from background carriers (i.e., produced by the ionization of defects other than the qubit NV [11]), and p is a Boolean stochastic variable associated with the probability of finding the qubit NV in the negatively charged state prior to SCC. Finally, $t_{AID} = t_{SCC} + t_e + (t'_{ia} + t'_{ra})/n$ is the average time per repeat during AID, calculated as the sum of contributions from the SCC light pulse duration t_{SCC}, the spin evolution time t_e during the chosen protocol, and the ancilla traps charge initialization and readout times, t'_{ia} and t'_{ra}, respectively.

Depending on the fidelity of the SCC process and the ancilla brightness, we identify different, complementary regimes: For example, assuming, for simplicity, $\langle\lambda\rangle \sim \langle p\rangle \sim 1$ and in the limit where $\langle k_a\rangle^2 \sum_j \delta^2 v_j \gg \langle k_a\rangle \sum_j \langle v_j\rangle^2$ (typically corresponding to $\langle k_a\rangle \gg 1$), we obtain

$$\eta_{AID} \sim \frac{\sqrt{t_{AID}}\sqrt{\langle q_0\rangle(1 - \langle q_0\rangle) + \langle q_1\rangle(1 - \langle q_1\rangle)}}{|\langle q_0\rangle - \langle q_1\rangle|}, \quad (2)$$

dependent only on the qubit spin-to-charge conversion probabilities. Conversely, when $\langle k_a\rangle^2 \sum_j \delta^2 v_j \ll \langle k_a\rangle \sum_j \langle v_j\rangle^2$, the sensitivity can be written as

$$\eta_{AID} \sim \frac{\sqrt{t_{AID}}\sqrt{\langle q_0\rangle^2 + \langle q_1\rangle^2}}{|\langle q_0\rangle - \langle q_1\rangle|\sqrt{\langle k_a\rangle}}, \quad (3)$$

improving inversely with the SCC contrast and the square root of the number of photons collected during ancilla charge readout. Both limits are formally identical to those found in standard SCC-based detection, implying that AID shares the benefits of charge readout [24,25]. Importantly, however, the integrated nature of the AID detection removes the characteristic SCC time overhead so long as the ensemble initialization and readout times are sufficiently short. Furthermore, in the regime of Eq. (3), additional gain over SCC can be attained by choosing ancilla traps featuring photon emission rates exceeding that of the qubit, and/or with longer ionization-recombination times [11]. For an NV center acting as the spin qubit, this latter limit can be attained at low temperatures where optical transitions are spin selective [28] (thus facilitating efficient spin-conditional charge initialization and ionization, i.e., $\delta^2 v_j \sim 0$).

Our present experimental conditions are far from this ideal regime, partly because the time intervals required for point-by-point charge initialization and readout as implemented herein are intrinsically long. More importantly, background traps coexisting with the ancillas (such as nitrogen impurities as well as other types of variable-charge defects abundant in chemical-vapor-deposition diamond [29]) can trap spin-encoded carriers. Indeed, dynamic conversion from and to a starting charge state effectively reduces the number of signal-carrying charges able to activate additional ancilla defects, hence leading to a nonlinear, slower signal growth [as observed in Figs. 2(b) and 3(e)] and, thus, to a reduced SNR [11,30–32]. Note that optical excitation of background defects at the point of illumination can also produce informationless, background carriers whose capture by the ancilla traps negatively impacts the AID SNR. In the limit dominated by poor ancilla activation efficiency (i.e., $\langle\lambda\rangle \ll 1$) and multiple background carriers (i.e., $\langle w\rangle \gg \langle p\rangle\langle q_j\rangle$, $j = 0, 1$), Eq. (1) yields

$$\eta_{AID} \sim \frac{\sqrt{2t_{AID}}w}{\sqrt{\langle\lambda\rangle\langle p\rangle}|\langle q_0\rangle - \langle q_1\rangle|}, \quad (4)$$

where the advantages of integrated charge readout vanish (the case in this work).

Despite the present unfavorable conditions, there is much room for improvement as the location, concentration, and type of ancilla defects—here simply defined by the intrinsic conditions of our samples during crystal growth—can instead be separately optimized using existing defect engineering protocols. Future work can benefit from defect engineering and charge guiding, e.g., to suppress background carriers produced either during NV charge initialization or from ionization of other coexisting defects near the qubit site. By the same token, arrays of electrodes could be exploited to prevent unintended carrier trapping away from the target ancillas or to physically separate electrons and holes so as to double the integrated signal. Along the same lines, we note that, because photogenerated carriers diffuse in three dimensions (3D), the two-dimensional (2D) plots observed here contain only a fraction of the total spin signal.

Interestingly, AID and SOS are not mutually exclusive, as the latter can easily be made part of the former by recording the NV fluorescence during (a fraction of) the SCC pulse. By the same token, since the nuclear spin state of the host nitrogen is robust to NV^- ionization [19], repetitive nuclear spin readout schemes [33,34] can be adapted so as to enhance the number of carriers produced during each repeat via multiple runs of the SCC pulse in each repeat. Reading the spin state of the qubit defect through the fluorescence of an ancilla emitter separates spin qubit manipulation and readout into two independent processes that can be individually adjusted. The latter provides an intriguing route to more efficiently probe spin qubits with photon emission at inconvenient wavelengths (such as the SiV^0 in diamond), with a low quantum yield (such as rare earth ions), or with undesired phonon-shifted fluorescence (such as the NV).

Although qubit readout is the most obvious application, many of the ingredients that make the present results possible could also serve as a general platform to tackle problems of fundamental and applied interest. One intriguing possibility is the use of spin-selective defect ionization as a route for spin-polarized carrier injection, of interest for spintronics applications in systems such as diamond where the use of ferromagnetic electrodes is impractical [5]. Preliminary experiments in our labs suggest these ideas can be extended from ensembles to pairs of defects, one serving as the carrier source and the other as the target. Among other options, such sets could be exploited to measure capture cross sections at the level of individual spin qubits, to implement alternative forms of sensing, or to track carrier transport under the action of external forces.

[*]Corresponding author.
cmeriles@ccny.cuny.edu

[1] D. D. Awschalom, R. Hanson, J. Wrachtrup, and B. B. Zhou, Quantum technologies with optically interfaced solid-state spins, Nat. Photonics **12**, 516 (2018).

[2] C. L. Degen, F. Reinhard, and P. Cappellaro, Quantum sensing, Rev. Mod. Phys. **89**, 035002 (2017).

[3] E. Togan, Y. Chu, A. S. Trifonov, L. Jiang, J. Maze, L. Childress, M. V. G. Dutt, A. S. Sørensen, P. R. Hemmer, A. S. Zibrov, and M. D. Lukin, Quantum entanglement between an optical photon and a solid-state spin qubit, Nature (London) **466**, 730 (2010).

[4] B. Hensen, H. Bernien, A. E. Dréau, A. Reiserer, N. Kalb, M. S. Blok, J. Ruitenberg, R. F. L. Vermeulen, R. N. Schouten, C. Abellán, W. Amaya, V. Pruneri, M. W. Mitchell, M. Markham, D. J. Twitchen, D. Elkouss, S. Wehner, T. H. Taminiau, and R. Hanson, Loophole-free Bell inequality violation using electron spins separated by 1.3 kilometres, Nature (London) **526**, 682 (2015).

[5] M. W. Doherty, C. A. Meriles, A. Alkauskas, H. Fedder, M. J. Sellars, and N. B. Manson, Towards a Room-Temperature Spin Quantum Bus in Diamond via Optical Spin Injection, Transport and Detection, Phys. Rev. X **6**, 041035 (2016).

[6] M. Pfender, N. Aslam, P. Simon, D. Antonov, G. Thiering, S. Burk, F. Fávaro de Oliveira, A. Denisenko, H. Fedder, J. Meijer, J. A. Garrido, A. Gali, T. Teraji, J. Isoya, M. W. Doherty, A. Alkauskas, A. Gallo, A. Grüneis, P. Neumann, and J. Wrachtrup, Protecting a diamond quantum memory by charge state control, Nano Lett. **17**, 5931 (2017).

[7] B. J. Shields, Q. P. Unterreithmeier, N. P. de Leon, H. Park, and M. D. Lukin, Efficient Readout of a Single Spin State in Diamond via Spin-to-Charge Conversion, Phys. Rev. Lett. **114**, 136402 (2015).

[8] E. Bourgeois, A. Jarmola, P. Siyushev, M. Gulka, J. Hruby, F. Jelezko, D. Budker, and M. Nesladek, Photoelectric detection of electron spin resonance of nitrogen-vacancy centres in diamond, Nat. Commun. **6**, 8577 (2015).

[9] F. M. Hrubesch, G. Braunbeck, M. Stutzmann, F. Reinhard, and M. S. Brandt, Efficient Electrical Spin Readout of NV–Centers in Diamond, Phys. Rev. Lett. **118**, 037601 (2017).

[10] P. Siyushev, M. Nesladek, E. Bourgeois, M. Gulka, J. Hruby, T. Yamamoto, M. Trupke, T. Teraji, J. Isoya, and F. Jelezko, Photoelectrical imaging and coherent spin-state readout of single nitrogen-vacancy centers in diamond, Science **363**, 728 (2019).

[11] See Supplemental Material at http://link.aps.org/supplemental/10.1103/PhysRevLett.125.236601 for additional experimental details and modeling of detection sensitivity.

[12] A. Gali and J. R. Maze, Ab initio study of the split silicon-vacancy defect in diamond: Electronic structure and related properties, Phys. Rev. B **88**, 235205 (2013).

[13] S. Häußler, G. Thiering, A. Dietrich, N. Waasem, T. Teraji, J. Isoya, T. Iwasaki, M. Hatano, F. Jelezko, A. Gali, and A. Kubanek, Photo-luminescence excitation spectroscopy of

SiV$^-$ and GeV$^-$ color center in diamond, New J. Phys. **19**, 063036 (2017).

[14] S. Dhomkar, H. Jayakumar, P. R. Zangara, and C. A. Meriles, Charge dynamics in near-surface, variable-density ensembles of nitrogen-vacancy centers in diamond, Nano Lett. **18**, 4046 (2018).

[15] D. Bluvstein, Z. Zhang, and A. C. Bleszynski Jayich, Identifying and Mitigating Charge Instabilities in Shallow Diamond Nitrogen-Vacancy Centers, Phys. Rev. Lett. **122**, 076101 (2019).

[16] D. A. Hopper, R. R. Grote, S. M. Parks, and L. C. Bassett, Amplified sensitivity of nitrogen-vacancy spins in nano-diamonds using all-optical charge readout, ACS Nano **12**, 4678 (2018).

[17] I. Meirzada, Y. Hovav, S. A. Wolf, and N. Bar-Gill, Negative charge enhancement of near-surface nitrogen vacancy centers by multicolor excitation, Phys. Rev. B **98**, 245411 (2018).

[18] J. Choi, S. Choi, G. Kucsko, P. C. Maurer, B. J. Shields, H. Sumiya, S. Onoda, J. Isoya, E. Demler, F. Jelezko, N. Y. Yao, and M. D. Lukin, Depolarization Dynamics in a Strongly Interacting Solid-State Spin Ensemble, Phys. Rev. Lett. **118**, 093601 (2017).

[19] S. Dhomkar, J. Henshaw, H. Jayakumar, and C. A. Meriles, Long-term data storage in diamond, Sci. Adv. **2**, e1600911 (2016).

[20] M. W. Doherty, N. B. Manson, P. Delaney, F. Jelezko, J. Wrachtrup, and L. C. L. Hollenberg, The nitrogen-vacancy colour centre in diamond, Phys. Rep. **528**, 1 (2013).

[21] E. van Oort, N. B. Manson, and M. Glasbeek, Optically detected spin coherence of the diamond N-V centre in its triplet ground state, J. Phys. C **21**, 4385 (1988).

[22] N. Aslam, G. Waldherr, P. Neumann, F. Jelezko, and J. Wrachtrup, Photo-induced ionization dynamics of the nitrogen vacancy defect in diamond investigated by single-shot charge state detection, New J. Phys. **15**, 013064 (2013).

[23] D. A. Hopper, R. R. Grote, A. L. Exarhos, and L. C. Bassett, Near-infrared-assisted charge control and spin readout of the nitrogen-vacancy center in diamond, Phys. Rev. B **94**, 241201(R) (2016).

[24] D. A. Hopper, R. R. Grote, S. M. Parks, and L. C. Bassett, Amplified sensitivity of nitrogen-vacancy spins in nanodiamonds using all-optical charge readout, ACS Nano **12**, 4678 (2018).

[25] H. Jayakumar, S. Dhomkar, J. Henshaw, and C. A. Meriles, Spin readout via spin-to-charge conversion in bulk diamond nitrogen-vacancy ensembles, Appl. Phys. Lett. **113**, 122404 (2018).

[26] S. Dhomkar, P. R. Zangara, J. Henshaw, and C. A. Meriles, On-Demand Generation of Neutral and Negatively-Charged Silicon-Vacancy Centers in Diamond, Phys. Rev. Lett. **120**, 117401 (2018).

[27] H. Jayakumar, J. Henshaw, S. Dhomkar, D. Pagliero, A. Laraoui, N. B. Manson, R. Albu, M. W. Doherty, and C. A. Meriles, Optical patterning of trapped charge in nitrogen-doped diamond, Nat. Commun. **7**, 12660 (2016).

[28] A. Batalov, V. Jacques, F. Kaiser, P. Siyushev, P. Neumann, L. J. Rogers, R. L. McMurtrie, N. B. Manson, F. Jelezko, and J. Wrachtrup, Low Temperature Studies of the Excited-State Structure of Negatively Charged Nitrogen-Vacancy Color Centers in Diamond, Phys. Rev. Lett. **102**, 195506 (2009).

[29] A. Lozovoi, D. Daw, H. Jayakumar, and C. A. Meriles, Dark defect charge dynamics in bulk chemical-vapor-deposition-grown diamonds probed via nitrogen vacancy centers, Phys. Rev. Mater. **4**, 053602 (2020).

[30] L. S. Pan, D. R. Kania, P. Pianetta, and O. L. Landen Carrier density dependent photoconductivity in diamond, Appl. Phys. Lett. **57**, 623 (1990).

[31] M. Nesladek, A. Bogdan, W. Deferme, N. Tranchant, and P. Bergonzo Charge transport in high mobility single crystal diamond, Diam. Relat. Mater. **17**, 1235 (2008).

[32] J. Isberg, A. Tajani, and D. J. Twitchen, Photoionization measurement of deep defects in single-crystalline CVD diamond using the transient-current technique, Phys. Rev. B **73**, 245207 (2006).

[33] L. Jiang, J. S. Hodges, J. R. Maze, P. Maurer, J. M. Taylor, D. G. Cory, P. R. Hemmer, and R. L. Walsworth, A. Yacoby, A. S. Zibrov, and M. D. Lukin, Repetitive readout of a single electronic spin via quantum logic with nuclear spin ancillae, Science **326**, 267 (2009).

[34] P. Neumann, J. Beck, M. Steiner, F. Rempp, H. Fedder, P. R. Hemmer, J. Wrachtrup, and F. Jelezko, Single-shot readout of a single nuclear spin, Science **329**, 542 (2010).